Applied Catalysis B: Environmental 250 (2019) 171–180

Contents lists available at ScienceDirect

Applied Catalysis B: Environmental

journal homepage: www.elsevier.com/locate/apcatb

Engineering organic/inorganic hierarchical photocathode for efficient and stable quasi-solid-state photoelectrochemical fuel cells

Yanhu Wang, Huihui Shi, Kang Cui*, Jinghua Yu*

School of Chemistry and Chemical Engineering, University of Jinan, Jinan 250022, China

ARTICLE INFO

Keywords:
Quasi-solid-state
Photoelectrochemical fuel cell
pTTh-Cu_2O
Au-TiO_2 NRAs

ABSTRACT

Photoelectrochemical fuel cells (PFCs) serve as a model system for harvesting electric energy from solar and biomass based on anodic fuel oxidation and cathodic oxygen reduction reaction (ORR). However, the sluggish ORR thereby limits the performance of PFC. Herein, we present a novel photocathode with polyterthiophene (pTTh) coated p-type cuprous oxide (Cu_2O) (pTTh-Cu_2O) that achieves boosted ORR kinetics, as well as exhibits remarkably improved photostability. By utilizing a hydrogel electrolyte which can avoid the leakage and volatilization of liquid electrolyte, a quasi-solid-state PFC device with eminent stability that consists of gold nanoparticles (Au NPs) decorated TiO_2 nanorod arrays (Au-TiO_2 NRAs) photoanode and pTTh-Cu_2O photocathode can be assembled. And the fabricated PFC exhibits outstanding performance that yields an open circuit voltage of 0.78 V and a maximum power density of 130 $\mu W \cdot cm^{-2}$ utilizing glucose as feeding under illumination. Furthermore, the as-prepared quasi-solid-state PFC demonstrates its potential for practical application by lighting a commercial light-emitting diode (LED). It is our believe that such rational design not only can be expanded for organic wastes degradation and water splitting, but also shed a light on the development of portable electronics driven by solar.

1. Introduction

The increasing energy depletions and environment crisis have aroused considerable attention in the exploitation of renewable clean energy sources. Efficient utilizing the solar energy is regarded as the most promising candidate to address the challenge in sustainable global development [1–3]. Especially, the photoelectrochemical fuel cells (PFCs), usually composed of a photoanode, electrolyte and a cathode, tailoring solar energy and biomass conversion into electricity output, can be a desirable option to solve the energy crisis, as well as solutions to alleviate the pressures of environmental protection [4–11]. However, the major challenges currently remaining in the PFC system are the slow oxygen reduction reaction (ORR) occurred at cathode and the long-term stability problem caused by the leakage of liquid electrolytes [12,13].

To overcome the sluggish kinetics of ORR on cathode, scientists have been making tremendous efforts on exploring available electrocatalyst, such as platinum catalyst due to their enhanced activity and acceptable stability. Despite the best performance of platinum cathodic catalyst achieved hitherto, the high cost and scarcity of platinum constitute the obstacle in the drive for scale-up applications [14]. Therefore, to improve the ORR kinetics, efforts are being focused in a main direction searching for new materials and systems. Photo-assisted ORR activity coupled a metal semiconductor cathode, playing an important role in ORR for both photocatalytic and photoelectrochemical (PEC) approaches, has attracted much attention due to its environmental friendliness and cost-effective property [9,13,15–18]. Especially, cuprous oxide (Cu_2O), as a naturally abundant and low cost p-type semiconductor, is regarded as a promising candidate in solar energy conversion applications because of its negative conduction band (CB) and small band gap, which enable the production of high-potential electrons under irradiation [19,20]. Nonetheless, the major drawbacks that Cu_2O undergoes short electron diffusion and notorious photo-instability under irradiation potentially limits its large-scale utilization [21,22]. Thus, the critical problems for developing high performance Cu_2O based photocathode are attenuating the degeneration and charge recombination of Cu_2O. To address those issues, an attractive strategy is to adopt a suitable protection layers with favorable energy band position coating on Cu_2O [23]. Till now, various inorganic materials (such as ZnO, TiO_2 and NiO et al) have typically been employed to protect the Cu_2O from photo-corrosion [21,24–27]. And desired anti-corrosion has been greatly promoted, yet the major problem it faces is the poor electrical conductivity. Taking account of the above problem, conducting polymers with well chemical stability, electrical conductivity

* Corresponding authors.
E-mail addresses: chm_cuik@ujn.edu.cn (K. Cui), chm_yujh@ujn.edu.cn (J. Yu).

https://doi.org/10.1016/j.apcatb.2019.03.022
Received 20 November 2018; Received in revised form 5 March 2019; Accepted 8 March 2019
Available online 12 March 2019
0926-3373/

and photoelectrocatalytic activity may offer a promising opportunity in the fabrication of hybrid Cu_2O photocathodes. [28] Recently, polyterthiophene (pTTh), as a typical p-type organic semiconductor with comparable catalytic ability and photophysical property, has been investigated for application in efficient light-enhanced ORR [13,15,29,30]. Moreover, the pTTh can be easily incorporated with other semiconductors, which significantly promoted the PEC performance. As a result, the introduction of pTTh into Cu_2O forming a type II heterostructure would be one of the most effective strategies to extend its photocatalysis and photostability, and eventually improve the ORR kinetics of PFC system.

To meet the stability criteria for outdoor use of PFC, the long-term stability problem caused by liquid electrolytes such as the leakage and volatilization of solvents should be addressed. In responses to it, solid-state and quasi-solid-state electrolytes have been made to develop alternatives to liquid electrolytes [31,32]. Compared with solid-state electrolytes, the quasi-solid-state electrolytes not only possess high ionic conductivity but good interface contact with photoelectrodes as well [33]. Hence, the preparation of a quasi-solid-state hydrogel with high ionic conductivity, good interfacial filling properties to substitute liquid electrolyte provides a promising solution to solve the existing long-term stability and security issues.

Herein, a quasi-solid-state PFC device configured with Au NPs modified TiO_2 nanorod arrays (Au-TiO_2 NRAs) photoanode and Cu_2O-pTTh photocathode based on hydrogel films electrolyte was proposed (Scheme S1). During the working process, light driven fuel (glucose) oxidation was achieved by the quasi-solid-state PFC device with two photoactive electrodes. Employing Au-TiO_2 NRAs as photoanode facilitates the reaction efficiency for light driven fuel oxidation. The novel Cu_2O-pTTh photocathode allows for enhanced photocatalytic ability and photostability. Then, a hydrogel film served as the fuel reservoir for the package of electrolyte and fuel was prepared, ensuring the ion-conduction between photoanode and photocathode and eliminating the necessity of electrolytic cell. The assembled tandem PFC device with photoanode, photocathode and hydrogel enables the simultaneous utilization of solar and biomass energy, showing promising potential for applications in energy conversion. In addition, the electricity output can be further used as a sign for cell function when accompanied by a detector such as a light-emitting diode (LED) light or a multimeter. The developed tandem PFC would be further applied in efficiently degrading organic wastes or photocatalytic overall water splitting.

2. Experiment section

2.1. Preparation of Au-TiO_2 NRAs photoanode

TiO_2 NRAs were first grown over fluorine doped tin oxide (FTO) substrates via a hydrothermal method with modification [34]. A total of 10 mL ultrapure water and 10 mL concentrated HCl were mixed together and stirred for 10 min. Then, 0.4 mL aliquot of titanium butoxide was added into the above solution with another 30 min stirring to form a homogeneous mixture. After that, the homogeneous solution was transferred into a steel lined Teflon autoclave (25 mL capacity) and a piece of FTO substrates were placed at an angle against the inner wall of the autoclave, with the conductive side facing down toward the wall of the Teflon liner. Then the autoclave was sealed and heated to 150 °C in an oven, held at the temperature for 4 h to facilitate the growth of the TiO_2 NRAs. After cooling to room temperature, the FTO substrate was removed from the autoclave, washed with ultrapure water and absolute ethanol, followed by drying in ambient air. Finally, the FTO substrates were annealed at 500 °C for 2 h to improve the crystallinity. Then Au NPs were deposited on pre-synthesized TiO_2 NRAs via a facile ionic layer adsorption and thermal-reduction method. The TiO_2 NRAs were first soaked in 1 mM aqueous $HAuCl_4$ for 30 min and dried under N_2 flow. Then transferred into a 50 mL mixture solution of ethanol and ultrapure water (v:v = 2:3) heating to boiling for 1 h to reduce the absorbed Au^{3+} to Au° at the sacrifice of ethanol. Finally, after rinsing with ultrapure water and dried in N_2 stream, the Au NPs modified TiO_2 NRAs (Au-TiO_2 NRAs) photoanode were obtained.

2.2. Preparation of pTTh-Cu_2O photocathode

An electrochemical deposition method was adopted to assemble Cu_2O on the FTO substrate accorfing to previous work with modifications [22]. Precursor solution containing 0.3 M $CuSO_4$ and 3 M lactic acid was firstly prepared, and then the pH of precursor solution was adjusted to 12 by 4 M NaOH solution. Electrodeposition was performed under potentiostatic potential of -0.4 V in a three-electrode system with FTO as working electrode, saturated Ag/AgCl as reference electrode and Pt as counter electrode at 60 °C. After 30 min deposition, a photoactive Cu_2O film was deposited on the FTO substrate. The polyterthiophene (pTTh) was in suit polymerized on Cu_2O film by CV processed in acetonitrile solution containing 10 mM 2,2,5,2-terthiophene (TTh) and 0.10 M $LiClO_4$ using a three electrode cell with a potential ranging from 0 to 1.2 V at a scan rate of 25 $mV{\cdot}s^{-1}$.

2.3. Preparation of hydrogel films

For the hydrogel films preparation, first, 2-acrylamido-2-methlypropane (AMPS, 1 M), N, N-methylenebisacrylamide (MBAA, 40 mM), 2-oxoglutaric acid (OA, 1 mM) and ammonium persulfate (APS, 19 mM) were mixed and moved into a silicone mold heating to 70 °C in an oven for preliminarily crosslink reaction. After that, the formed soft gel was immersed into a mixture solution containing acrylamide (AAm, 4 M), OA (1 mM), NaCl (80 mM) and APS (19 mM) for another 10 h. Then the gel film was washed with ultrapure water and subsequently immersed into a mixture solution with AAm (2 M), OA (1 mM) and APS (19 mM) for another 10 h under UV irradiation. After washing with water overnight, the obtained hydrogel film was following immersed into 0.1 M phosphate buffered saline (PBS) (pH 7.0) containing 50 mM glucose for efficient fuel absorption by 24 h. As shown in Fig. S1 A, a transparent hydrogel film was obtained. Scanning electron microscopy (SEM) image in Fig. S1B shows that abundant pores with a diameter of 100 nm presented on the surface of hydrogel film, which are favorable for liquid electrolyte absorbing and retaining.

2.4. PFC assembly and performance

For PFC assembled, the Au-TiO_2 NRAs photoanode and pTTh-Cu_2O photocathode were laminated to the same side of the hydrogel sheet (Scheme S1). The light source (500 W Xe lamp) was equipped at the front of the electrodes in order that the luminous beam can vertically hit the electrode surface under ambient air at room temperature.

3. Results and discussion

3.1. Materials characterization

Fig. S2 presents the design and fabrication strategies for the Au-TiO_2 NRAs photoanode. TiO_2 NRAs aligned on FTO substrate was first synthesized by a simple hydrothermal reaction, further functionalized by Au NPs through ionic layer adsorption and thermal-reduction approach. The top and cross section view SEM images of the prepared TiO_2 NRAs in Fig. 1A corroborate the smooth surfaces of TiO_2 NRAs assembled on the FTO substrate. The diameter and length of nanorods were around 100 nm and 1 μm respectively, consistent with that observed by transmission electron microscopy (TEM) (Fig. S3 A). After Au NPs decoration, the TiO_2 NRAs still maintained their vertically orientated characteristics due to the small size of Au NPs (Fig. 1B), but with the color changing from creamy white to dark grey (inset in Fig. 1A and B). Furthermore, TEM image in Fig. S3B clearly revealed that large amount of Au NPs with an average size of 5 nm uniformly distributed on the

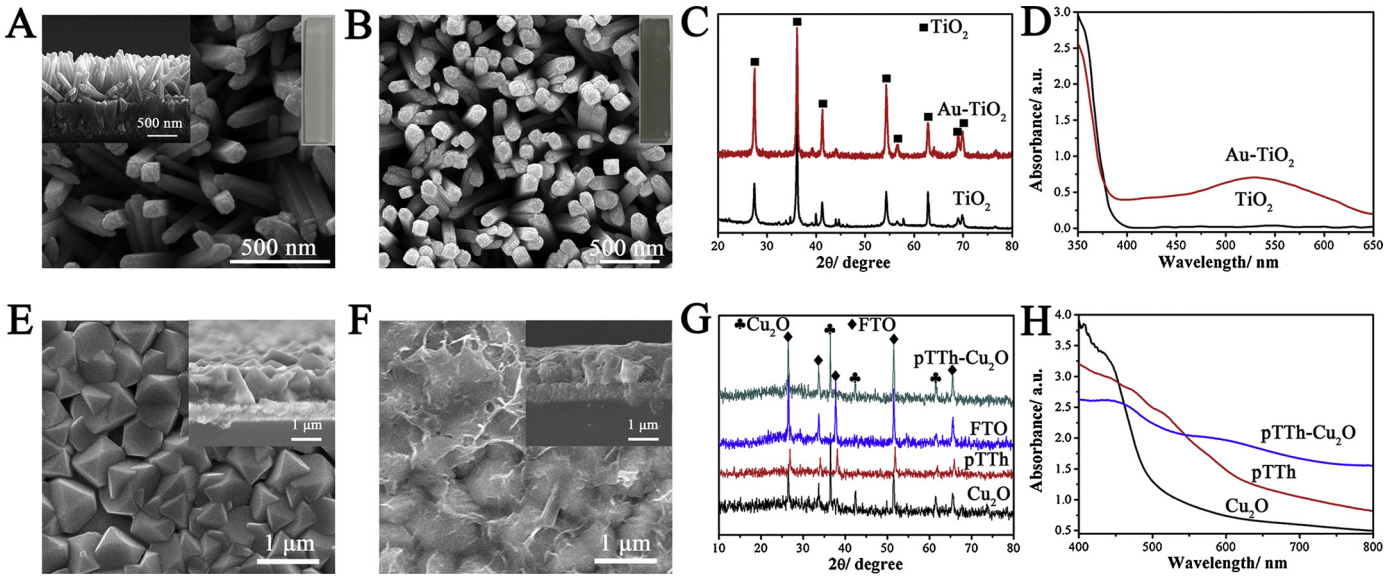

Fig. 1. Top-view SEM images of TiO_2 NRAs (A), Au-TiO_2 NRAs (B), Cu_2O (E) and pTTh-Cu_2O (F); X-ray diffraction (XRD) patterns (C and G) and UV–vis spectra (D and H) for different prepared photoanode (C and D) and photocathode (G and H); inset is the cross-sectional SEM image of TiO_2 NRAs (A), Cu_2O (E) and pTTh-Cu_2O (F) and photographs of as-prepared TiO_2 NRAs (A), Au-TiO_2 NRAs (B).

surface of TiO_2 nanorod. And the uniform functionalization of Au NPs on the surface of TiO_2 nanorod can effectively prevent recombination between the photo-generated charge carriers and consequently, resulting in a significant improvement in PFC efficiency. The high-resolution TEM (HRTEM) image reveals the highly crystalline Au NPs and TiO_2. Well-resolved lattice fringes of 0.20 and 0.24 nm can be indexed to the (200) and (111) planes of Au NPs (Fig. S3C) [35]. And TiO_2 dispalys a lattice spacing of 0.32 nm consistent with the tetragonal rutile phase (Fig. S3D), confirming that the nanorod is single-crystalline [34], which would be favorable for electron transport. Additionally, the energy-dispersive X-ray spectrometer (EDS) and elemental mappings analysis (Fig. S4) also confirms the successful fabrication of Au-TiO_2 NRAs, in which the Ti, O and Au signals appear.

The phase components of as-synthesized products are revealed in the X-ray diffraction (XRD) patterns in Fig. 1C. The collected XRD diffraction peaks matched well with the characteristic peaks of rutile TiO_2 (JCPDS No. 02-0494). And the sharp and strong characteristic peaks reflect the high crystallinity of the as-prepared rutile TiO_2 which would facilitate photogenerated charge carriers transfer [36,37]. For comparison, no additional peaks could be observed for the Au-TiO_2 NRAs composites owning to the low amount of Au NPs compared with TiO_2. UV–vis spectra were employed to investigate the optical properties of the samples (Fig. 1D). The pristine TiO_2 NRAs exhibits a steep absorption edge occurred around 395 nm corresponding to the band-gap (˜3.1 eV) [38]. After the decoration of Au NPs, a much strong visible light absorption capability was obtained, which is favorable for utilizing solar energy and improving photocatalytic activity. The enhanced light absorption could be associated with the light absorption band red-shift of the Au NPs [39]. The results confirm that the optical-response property of photoanode can be effectively enhanced after the incorporation of Au NPs with TiO_2 NRAs.

Pyramid-like Cu_2O were prepared by the electrochemical deposition on FTO substrates. To improve the light absorption efficiency, charge transporting ability and photo-stabilities of photocathode, a layer of pTTh was deposited on the surface of Cu_2O through in situ electropolymerized TTh. As illustrated in Fig. 1E, well-developed cubes with discernible edges were observed, and the Cu_2O cubes ranges in size distribution around 500 nm could be seen. From the cross-sectional SEM image (inset in Fig. 1E), a dense and continuous film with special raised units can be observed with a thickness about 500 nm. The rough film affords superior light-harvesting characteristics, large contact areas with the electrolyte, and highly conductive pathways for separation and transport of charge carriers [40]. Compared with bare Cu_2O, a blurry but uniform film with many wrinkles was observed on Cu_2O surface after pTTh coating (Fig. 1F). The cross-sectional SEM image (inset in Fig. 1F) shows that the overlayer not only cover the grains of Cu_2O and filled their boundaries suggesting efficient protection fo Cu_2O stack, also confirms the successful preparation of pTTh-Cu_2O. The elemental mapping (Fig. S5) revealed the coexistence of Cu, O, C and S elements. Note that the homogeneous distribution of S and C demonstrated the uniformly coating of pTTh on Cu_2O surface.

The phase components of as-synthesized different types of photocathodes are revealed in the XRD patterns in Fig. 1G. It is observed that the Cu_2O displayed a typical reflection pattern of cuprite (JCPDS No. 77-0199) with four diffraction peaks corresponding to (111), (200), (211) and (311) locate at 36.6°, 42.3°, 61.4° and 74.2° [41]. No other diffraction peaks can be seen indicating that the high purity of Cu_2O. Meanwhile, the same diffraction peaks before and after electrodeposition of pTTh on FTO suggested the amorphous feature of pTTh. It can be seen that no phase change is observed after coating with pTTh on the surface of Cu_2O, which also confirms that the pTTh is amorphous. It speculates that the successful preparation of amorphous pTTh on Cu_2O, which would have a positive influence on the performance of photocathode. UV–vis absorption measurements were carried out to investigate the light-harvesting ability of the pTTh-Cu_2O photocathode (Fig. 1H). A sharp absorption band with the absorption edge near to 600 nm is observed which is corresponding to the band gap energy of Cu_2O (~2.1 eV) [22,42]. The light absorption edge for pTTh is estimated to be 620 nm. After pTTh assembled on Cu_2O, the absorption in the wavelength range exhibited a redshift compared with bare Cu_2O which was arose from the intrinsic band gap absorption of pTTh to facilitate the absorption of the solar energy.

Furthermore, X-ray photoelectron spectroscopy (XPS) was applied to provide deep insight into the surface chemical compositions and bonding states of Au-TiO_2 NRAs and pTTh-Cu_2O. The survey XPS spectra in Fig. 2A provided the Ti, O, C and Au peaks for Au-TiO_2 NRAs as well as Cu, O, C and S chemical binding energies for pTTh-Cu_2O (Fig. 2E), while no other impurity elements presented, suggesting the high purity of the as-prepared Au-TiO_2 NRAs and pTTh-Cu_2O. High-resolution XPS patterns of the Ti 2p and O 1 s peaks for the as-prepared TiO_2 NRAs are presented in Fig. 2B and 2C. Two bands located at 458.58 and 464.03 eV, are assigned to Ti 2p3/2 and Ti 2p1/2 spin-

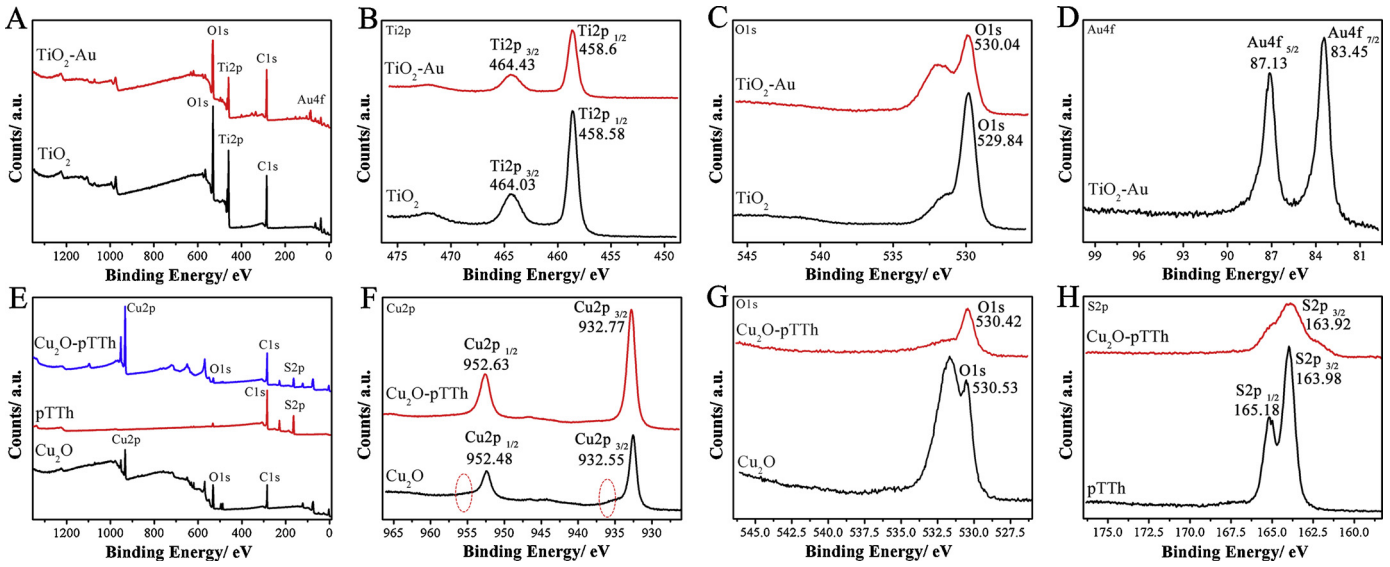

Fig. 2. Full scan XPS spectrum of photoanode (A) and photocathode (E) with corresponding narrow scan XPS spectra of (B) Ti 2p, (C) O 1 s (photoanode), (D) Au 4f, (F) Cu 2p, (G) O 1 s (photocathode) and (H) S 2p regions.

orbital splitting photoelectrons, and the distance between two peaks is about 5.45 eV are in good agreement with that in rutile TiO_2 [43]. The O 1 s peak centered at around 530.3 eV (Fig. 2C) is attributed to the binding energy of O_2 in the TiO_2 lattice, which is due to the Ti—O band [43]. Meanwhile, discernable shoulders around 531.43 eV were observed for both TiO_2 and Au-TiO_2 for O 1 s region, which might belong to surface hydroxyl group [44,45]. It was reported that the Au 4f spectrum (Fig. 2D) reveals the peaks at the binding energy of 83.45 eV (Au 4f7/2) and 87.13 eV (Au 4f5/2) from the metallic state Au [46,47]. However, a significant negative shift (ca. 0.55 eV) of the binding energy for Au 4f7/2 relative to 84.0 eV of the bulk Au is identified (Fig. 2D), which might be due to the electron transfer from oxygen vacancies of the TiO_2 to Au, leading to a lower Au 4f7/2 core level binding energy in the Au-TiO_2 NRAs. Compared to those of pure TiO_2 NRAs, a small positive shift of the Ti 2p3/2 (from 458.58 eV to 458.6 eV) and O 1 s (from 529.84 eV to 530.04 eV) after Au loading also reveals feasibility of the electron transfer between the Au and TiO_2 NRAs (Fig. 2B and C) [48].

From Fig. 2E, only peaks characteristic of Cu 2p, O 1 s, and C 1 s can be observed for Cu_2O. Compared with Cu_2O, the binding energy peaks of additional S elements can be detected in the pTTh-Cu_2O, which verifies the formation of target phtotcathode. The two peaks located at around 932.55 and 952.48 eV are assigned to the binding energy of Cu 2p3/2 and Cu 2p1/2, respectively, indicating the presence of the Cu^+ on the Cu_2O (Fig. 2F) [49]. A very slight shoulder is observed off the main Cu 2p peaks and the presence of small features between 938–948 eV and 958–968 eV in our spectra suggests slight surface oxidation of the sample [50]. For comparison, no “shake-up” satellite peaks at higher binding energies relative to the main Cu 2p 3/2 and Cu 2p 1/2 peaks in CuO could be seen for pTTh-Cu_2O, exhibited remarkably improved stability after pTTh coating. The O 1 s spectra shown in Fig. 2G exhibits a broad feature centered at 531 eV with a discernable shoulder at lower binding energies (530.53 eV). Deconvolution of this main feature suggests a contribution from the O atoms in the Cu_2O lattice itself (530.53 eV) and those O atoms are ascribed to the hydroxyl groups (531.61 eV) similar to O 1 s region from photoanode (Fig. 2C) [44,50,51]. After pTTh modification, the peak of O atoms related to surface hydroxyl group decreased and a discernable shoulder at higher binding energies. This feature is very similar to that previously reported for C-coated Cu_2O nanowires [51], and we therefore attribute the phenomenon to the interaction between O in Cu_2O and C from pTTh. As for bare pTTh, two peaks of 163.98 eV and 165.18 eV might be assigned to the S 2p3/2 and S 2p1/2 peaks (Fig. 2H). The intensity ratio is about 1:2 and their separation energy is around 1.2 eV, in good agreement with previously reported data [52]. In contrast, for pTTh-Cu_2O fitted peaks are shifted to more negative binding energies, and the S 2 P peaks obtained from pTTh-Cu_2O is broadened, and the peak located at 165.18 eV became weak, which may be ascribed to the bonding between S and Cu (Fig. 2H), also revealed the pTTh layer were deposited on the surface of Cu_2O successfully. In addition, it is noteworthy that, compared with Cu_2O the binding energy of Cu 2p3/2 was positively shifted (from 932.55 eV to 932.77 eV) after pTTh coating, whereas, the binding energy of S 2p3/2 negatively shifted (from 163.98 eV to 163.92 eV), which may originate from the strong interaction between Cu^+ and the protective layer, thereby indicating a close contact between Cu_2O and pTTh.

Meanwhile, the valence band levels of TiO_2, Cu_2O and pTTh were determined based on the linear extrapolation of the valence-band-edge spectra measured by XPS (Fig. S6). The band-gap energy was estimated to be 2.5 eV for TiO_2, 0.4 eV for Cu_2O and 1.85 eV for pTTh, consistent with the reported value of valence band [13,53,54]. And the conduction band was around -0.7 eV, -1.7 eV and -0.2 eV for TiO_2, Cu_2O and pTTh. The corresponding band energy-level alignment diagram of Cu_2O with pTTh was constructed as shown in Fig. S7.

3.2. Photoelectrocatalytic activity characterization

Glucose was selected as fuel to investigate the photoelectrocatalytic performance of Au-TiO_2 NRAs photoanode. Linear sweep voltammetry (LSV) experiments were carried out to evaluate the photoelectrocatalytic properties of photoanodes toward glucose oxidation. Fig. 3A showed the LSV curves of TiO_2 NRAs and Au-TiO_2 NRAs under different conditions. In the presence of glucose, negligible dark current were observed for both TiO_2 NRAs and Au-TiO_2 NRAs indicating that the photoelectric conversion resulting current response [28]. Under illumination, anodic current is observed with an onset potential at about -0.38 V (vs. Ag/AgCl) for TiO_2 NRAs. Importantly, the Au-TiO_2 NRAs photoanode yields larger anodic photocurrent output as well as cathodically shifted glucose oxidation onset potential which might attribute to the surface plasmon resonance (SPR) enhancement of Au NPs causing “hot” electron injection from Au NPs to TiO_2 and capturing photogenerated holes from TiO_2, thereby suppressing charge recombination and reducing the kinetic barrier for glucose oxidation [55]. While for Au-TiO_2 NRAs photoanode, lower anodic photocurrent is observed in the absence of glucose, with the onset potential positive

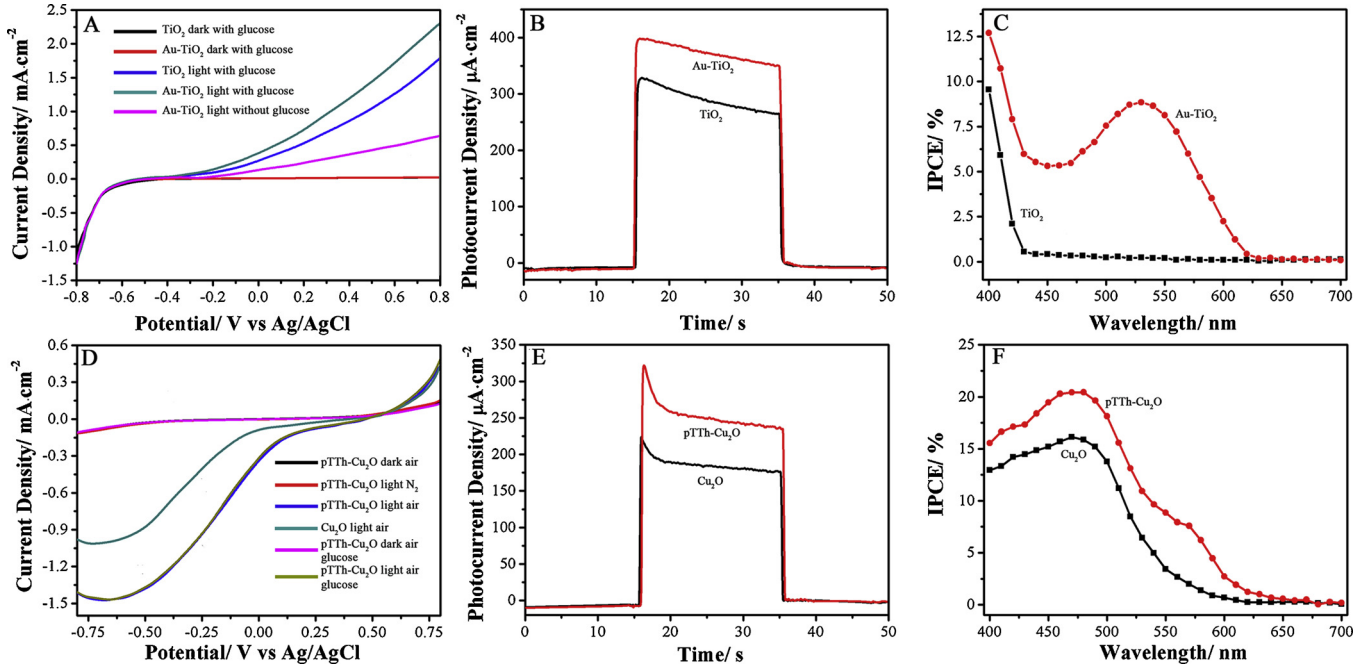

Fig. 3. LSV scans (A and D), transient photocurrent responses (B and E) and incident photon-to-current conversion efficiency (IPCE) (C and F) of prepared photoanode (A, B and C) photocathode (D, E and F) under different condition, scan rate 1 mV/s for LSV scanning, IPCE spectra of samples measured in 0.5 M Na_2SO_4 at a voltage of 0 V vs RHE.

shifted under illumination. These results indicate the Au-TiO_2 NRAs can be employed as an effective photoanode toward glucose oxidation.

Transient photocurrent responses were carried out to evaluate the effect of surface treatment of photoanode (Fig. 3B), consisting of the as-fabricated photoanode as the working electrode, Ag/AgCl as the reference electrode, the platinum wire as the counter electrode, and 0.1 M PBS containing 50 mM glucose as the electrolyte at pH 7. Once exposed to illumination, a sudden increase in the photocurrent could be seen for both the TiO_2 NRAs and Au-TiO_2 NRAs. And Au-TiO_2 NRAs displayed higher photocurrent response indicating an improvement in the photocurrent conversion efficiency of Au-TiO_2 NRAs by the addition of Au NPs, which could be originated from the improvement of light absorption and the transfer of SPR induced hot electrons from Au NPs to the TiO_2 NRs.

While, Fig. 3D shows the photocatalytic behaviors of the Cu_2O and pTTh-Cu_2O photocathodes with or without simulated illumination at air or anaerobic condition. At air condition, for the pTTh-Cu_2O photocathode, photocurrent intensity is significantly improved once expose to irradiation compared with that response recorded in dark. Meanwhile, compared to Cu_2O photocathode, the catalytic current obtained form pTTh-Cu_2O photocathode was boosted from -1.0 $mA{\cdot}cm^{-2}$ to -1.45 $mA{\cdot}cm^{-2}$ accompanied an anodic shifted oxygen reduction onset potential. This enhancement is attributed to the improvement of light absorption, capability of pTTh cocatalyst to capture photogenerated electrons from Cu_2O, suppressing charge recombination as well as reducing the kinetic barrier for oxygen reduction. It is also observed that an significant enhanced cathodic catalytic current was obtained in air-saturated electrolyte than in N_2-saturated electrolyte, suggesting the intensive capability of the pTTh-Cu_2O to catalyze oxygen reduction upon light illumination [56]. Furthermore, in the presence of glucose at air condition, either expose to illumination or not, no obvious changes of onset potential and catalytic current is observed compared with that in the absence of glucose. Based on the above discussion, we have proposed a novel strategy to simultaneously improve the PEC stability and activity of photocathode.

To test PEC performance of fabricated photocathode under illumination, amperometric I-t curves in Fig. 3E were measured with an applying constant potential of 0 V. As comparison, with the coverage of pTTh on Cu_2O photocathode, higher photocurrent response is obtained. The result indicates that beneficial charge carrier separation is enabled in this system. Menawhile, is should be pointed out that the photocurrent of each sample rose to the peak value rapidly with light illumination. Thereafter it declined gradually until equilibrium was reached. The photocurrent jump was attributed to the inevitable electron/hole recombination [57,58]. In particular, the electrons most likely recombine with holes during transfer, thus leading to in a decay of photocurrent intensity. Once the generation rate and recombination rate attained equilibrium, a steady state photocurrent density was achieved [59].

To further explore the relationship between the improved PEC performance and the optical-response capability of obtained photoelectrodes, incident photon-to-current conversion efficiency (IPCE) measurement was carried in a three-electrode electrochemical system with applied bias of 0 V vs reversible hydrogen electrode (RHE). The IPCE is defined by following equation: $IPCE = (1240J_{current})/(\lambda P_{light}) \times 100\%$

where $J_{current}$ is the photocurrent density, λ is the incident light wavelength, and P_{light} is the incident light power density [60]. As shown in Fig. 3C, bare TiO_2 NRAs only exhibits PEC activity only in the UV region, and the IPCE values decrease to almost zero in the visible light region. While, Au-TiO_2 NRAs demonstrated better IPCE values than TiO_2 NRAs and significant enhanced IPCE at the wavelength corresponding to the Au NPs could be observed, which should be attributed to the improved light absorption efficiency. The IPCE results are exactly consistent with the improved optical absorption including increased absorbance and extended absorption region. As for the photocathode (Fig. 3F), pTTh-Cu_2O show substantially enhanced IPCE in the entire testing wavelength region because of the incorporation of pTTh could increase the photo active range of Cu_2O which is in accordance with the photocurrent results. The results suggest that the formation of heterojunction allows the resulting photocathode with suppressed recombination of the photogenerated electron-hole pairs that enables the improvement of photoelectrical performances.

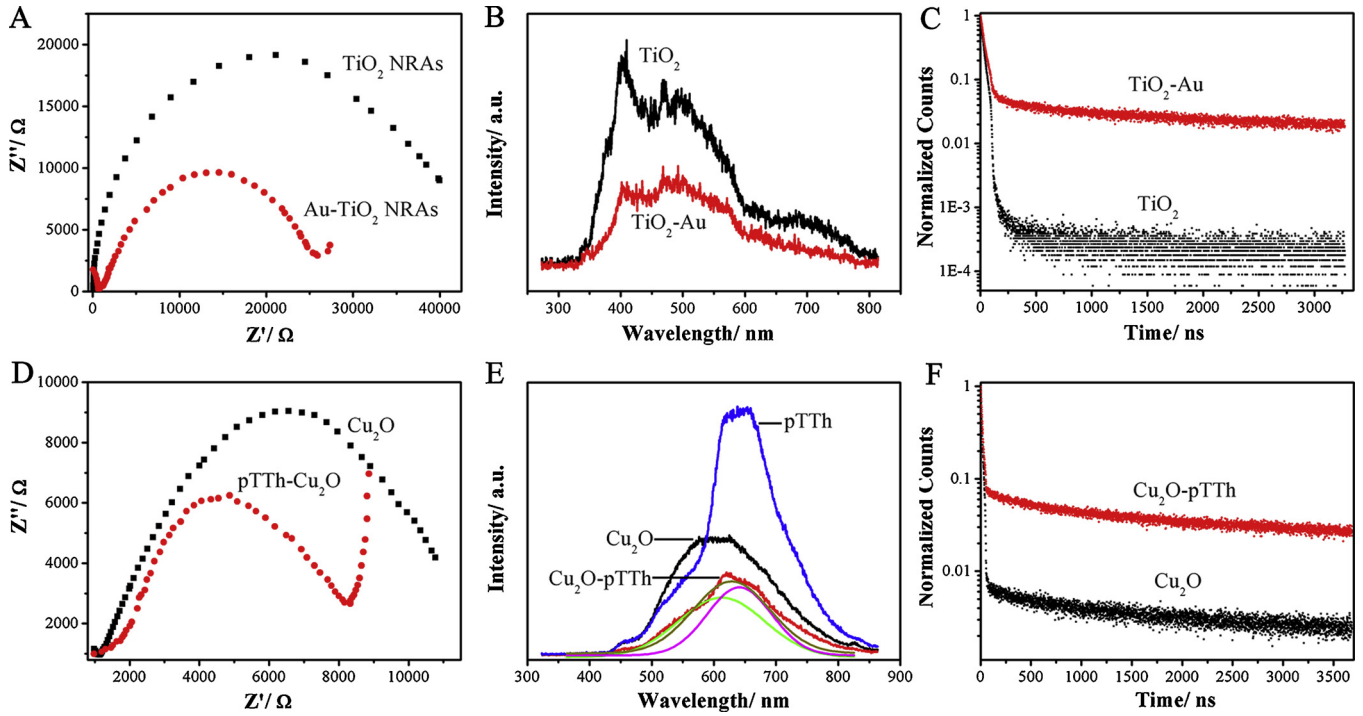

Fig. 4. EIS Nynquist plots (A and D), photoluminescence spectra (B and E) and time-resolved PL spectra (C and F) of photoanode (A, B and C) and photocathode (D, E and F), EIS Nynquist plots were measured under illumination.

3.3. Electrode kinetics

Electrochemical impedance spectroscopy (EIS) measurement carried out under illumination in a mixing electrolyte (5 mM $K_3Fe(CN)_6$, 5 mM $K_4Fe(CN)_6$ and 0.1 mM KCl) was further performed to gain deeper insight into the charge transfer behaviors of the as-prepared photoelectrodes. Smaller diameter of the semicircle means better carrier transfer performance, and the larger slope of the straight line indicates better interfacial charge transport kinetics [28,61]. The EIS Nyquist plots for photoelectrodes were collected at open-circuit conditions under simulated light illumination as shown in Fig. 4A and D. And the experimental data dots are fitted into solid lines using the equivalent circuit model in Fig. S8. Here, R_s is the series resistance of the electrochemical device, CPE and R_{ct} are the capacitance phase element and the charge transfer resistance across the photoelectrode/electrolyte interface, respectively. The lower resistance value should be ascribed to the formation of heterojunction interfaces and the enhanced charge carrier density under irradiation, eventually leading to improved PEC performance. Those consistent conclusions are exactly matched with that of photocurrent responses (Fig. 3B and E).

In addition to EIS, the photoluminescence (PL) spectra have been employed to investigate the charge carrier separation efficiency of the fabricated photoelectrodes. Lower PL intensity suggests a low density of recombination centers and consequently long lifetime of photogenerated carriers. The PL spectrum (Fig. 4B) for bare TiO_2 NRAs displays an intense, broad emission from 370 to 600 nm. It is obvious showed that the PL emission obtained from Au-TiO_2 NRAs quenched drastically, suggesting an efficient reduction in recombination of photoinduced charge carriers and consequently longer life of photogenerated carriers there [62]. Fig. 4E presents the PL spectra of the prepared photocathode. PL measurements for pure Cu_2O revealed a strong PL peak around 600 nm. And the bare pTTh present the strong PL intensity with the peak located at 640 nm. In contrast, the pTTh-Cu_2O (brown line denoted as the fitted pTTh-Cu_2O PL spectrum) possesses a broad visible emission with a slightly redshift (centered at 620 nm) compared with that of pure Cu_2O. And Gaussian fit for the spectrum of pTTH-Cu_2O was adopted to identify the origin changes of the PL spectrum. The luminescence spectrum of pTTH-Cu_2O could be well fitted into two components: one is due to the luminescence of Cu_2O (green line) and the other related to pTTh (pink line). The changes of the spectrum might be attributed to the Coulomb interaction between pTTh and Cu_2O, as well as the fact that the multiexciton is actually a mixture of single, bi- and multiexcitons [63]. The above results indicate that after the formation of a pTTh layer on the surface, the nature of visible emission is changed. This phenomenon is similar to that of previously reported PbS-modified ZnS hollow microspheres [64]. And the diminishment of PL peak intensity suggested the repressed recombination of photoinduced electrons and holes in pTTH-Cu_2O.

In order to further illustrate the lifetimes of photogenerated carrier in the excited state for all samples, time resolved PL spectra are performed. As for the Au-TiO_2 NRAs (Fig. 4C), the carrier lifetime increased from 2.71 ns to 4.08 ns compared with pristine TiO_2, indicating a much more efficient carrier separation performance [65]. And the result is similar to photocathode (Fig. 4F), the fluorescence lifetime values were determined to be 3.87 and 6.88 ns for Cu_2O and pTTh-Cu_2O respectively, through the equation: $\tau = (B_1\tau_1^2 + B_2\tau_2^2)/(B_1\tau_1 + B_2\tau_2)$. The related time constant and calculated average lifetime are listed in Table S1 (Supporting Information). The increased fluorescence lifetime might suggest that the separated charge carriers live longer and have more probability of transferring to the catalyst surface to participate in the redox reactions [66].

3.4. Performances of the as-assembled light driven PFC

PFC offers an attractive way to simultaneously convert solar and biomass energy into electricity. And open-circuit voltage (V_{oc}) was selected to investigate the photoelectric properties of the designed PFC systems. As shown in Fig. 5A, the V_{oc} variation tendency of photoanode, photocathode and the assembled PFC in 50 mM glucose were recorded under 500 W Xe lamp irradiation. It was found that no obvious change was observed for the Au-TiO_2 system. While significant change was occurred as for the pTTh-Cu_2O system. Based on those, the V_{oc} response of assembled tandem PFC was instant increased from 0.08 to 0.78 V as

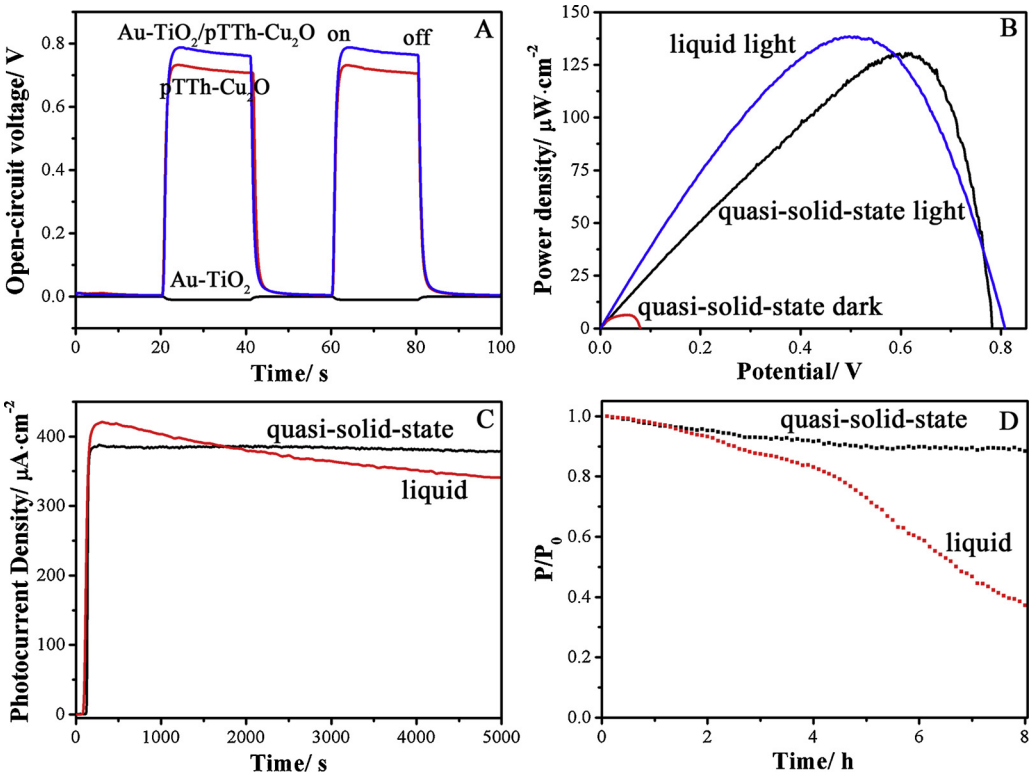

Fig. 5. (A) the open-circuit potential of the photoanode, photoathode and assembled PFC under illumination; (B) dependence of the power output on the PFC voltage under illumination and dark using different electrolytes; (C) photocurrent stability measurement and (D) time-course changes of the power output ratio (P/P_0) of the PFC with quasi-solid-state and liquid electrolyte.

expose to illumination, validating the conversion of solar and chemical energy into electricity. And the mismatching Fermi levels of the two photoelectrodes that favourable for charge transfer would be account for the photovoltage [54,67,68]. Fig. 5B also shows the performance characteristics of the assembled PFC device. With illumination, the maximum power output of the quasi-solid-state PFC reached 130 $\mu W \cdot cm^2$ at +0.6 V much higher than that without illumination. Only a little lower open-circuit voltage and power density output was obtained for quasi-solid-state PFC than that of PFC containing liquid electrolyte. The result demonstrated well interface contact between quasi-solid-state electrolyte and photoelectrodes.

Meanwhile, stability of the assembled PFC device is also investigated through measuring photocurrent density-time curve (Fig. 5C). Spiked photocurrent appeared with light turning on. With extending to illumination time for 5000 s, the quasi-solid-state PFC exhibited a more stable photocurrent response compared with that PFC containing liquid electrolyte. Meanwhile, in a long-term continuing operation (8 h), the quasi-solid-state PFC showed a relatively slow decay of power output. On the contrary, there was an obvious power output change of the PFC using liquid electrolyte (Fig. 5D). All those results indicated the as-fabricated quasi-solid-state PFC device has decent stability, which is an important parameter for its practical application. In addition, the present PFC shows superior or comparable performance than previous reported PFC, even though the experimental conditions are different (Table S2).

Based on above results, the working principle of the as fabricated glucose fueled PFC was presented in Scheme 1. TiO_2 NRAs can be excited along with photoelectrons and holes generation on the CB and valence band (VB) upon illumination. Simultaneously, Au NPs anchored to the surface of TiO_2 NRAs exhibited plasmonic behavior consistent with the increased visible light absorbance. Under irradiation, hot electrons generated from surface plasmons photoexcition of Au NPs. Due to the higher surface plasmon states compared with the band level of TiO_2, the photo-induced hot electrons were transferred from the plasmonic metal to the conduction band of TiO_2 NRAs further collected by current collector and transmited to the cathode, while the

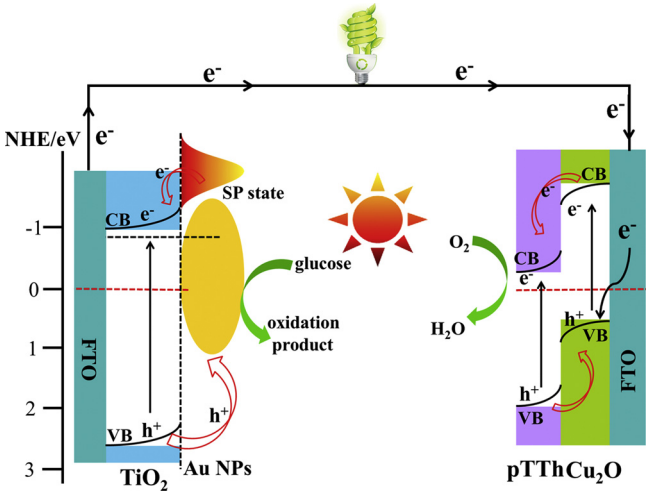

Scheme 1. Energy level diagram of the glucose fueled PFC.

holes are expelled to the Au NPs [69,70]. In such a process, both accumulation of photoelectrons and separation of the photo-excited carriers are accomplished, that are beneficial for improving the performance of photoanode. As for the photocathode, As for the photocathode, the type II heterostructure was formed as shown in Fig. S7. Under irradiation, photoinduced electrons formed both in the VB of pTTh and Cu_2O. Owning to the fact that the energy band of pTTh were more positive than Cu_2O, the photoexcited electrons in the CB of Cu_2O transfer directly to the CB of pTTh, whereas the holes in the VB of pTTh transfer to the VB of Cu_2O expeditiously; the holes are trapped by the generated photoelectrons from photoanode driven by the self-driven bias. These results can restrain photoinduced charge carrier recombination and improve the photocatalytic performance under irradiation. At the same time, photoinduced holes from TiO_2 NRAs leap into the Au NPs and photogenerated electrons accumulated on LUMO energy level of pTTh move to the semiconductor/electrolyte interface

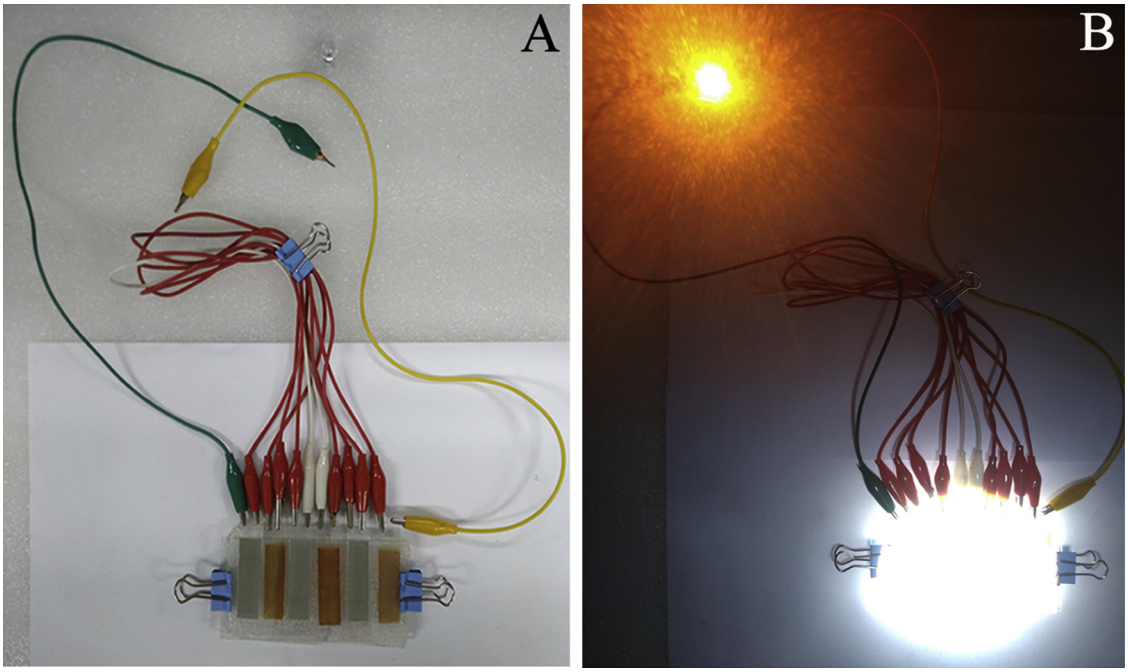

Fig. 6. (A) picture of three tandem PFCs and (B) a red light-emitting diode lighted by three individual PFC connected in series. (For interpretation of the references to colour in this figure legend, the reader is referred to the web version of this article).

respectively to attend the biomass derivatives oxidation reaction and oxygen reduction reaction.

In order to explore additional applications of the PFC device, series-wound PFCs were combined together to light up a red light-emitting diode (LED) (Fig. 6A). Under the illumination of simulated solar light, a signal PFC device can produce a maximum voltage of 0.78 V. Thus, serial PFCs were connected to power a LED directly under illumination (Fig. 6B). In this case, the amount of energy generation can be clearly indicated by the LED emission intensity. Based on this, the combination of the as-prepared PFC with energy storage devices together may provide a reasonable paradigm to reduce energy waste and minimize the additional components necessary [71,72].

3.5. Photocathode stability investigation

The effect of pTTh layer on the photostability of Cu_2O photocathode was examined by repeating the experiment several times under continuous illumination at 0 V vs Ag/AgCl. No noticeable photocurrent density degradation for both Cu_2O and pTTh-Cu_2O photocathode initially (Fig. 7A). After 2 weeks storage, the photocurrent response of Cu_2O photocathode without pTTh protective layer had a significant decline, while no noticeable degradation in the subsequent runs could be observed for the pTTh-Cu_2O photocathode. In addition, the photocatalytic stability of pTTh-Cu_2O for ORR was examined (Fig. 7B). After 2 weeks storage, the bare Cu_2O showed significant decrease ORR activity in air-saturated condition as well as the onset potential shifted to more negative values, whereas the pTTh-Cu_2O exhibited no obvious change with original samples. The stability for ORR catalyzed by Cu_2O and pTTh-Cu_2O were studied and compared at the potential of -0.5 V versus AgCl under air-aerating condition (Fig. 7C). The photocurrent decreased from -0.87 $mA{\cdot}cm^{-2}$ to -0.5 $mA{\cdot}cm^{-2}$ for Cu_2O, however, the pTTh-Cu_2O shows an excellent stability and only an approximately little decrease. The degradation of Cu_2O photocathode PEC performance is likely to be derived from the fact that the Cu^+ can be easily corroded [51,73]. While, the presence of pTTh layer effectively prevents the Cu_2O layer from contacting the interface as well as facilitates photogenerated electrons to drift from the Cu_2O into the semiconductor/electrolyte interface due to their matching conduction band position. The comparison between SEM images of two types photocathode upon the PEC test and after two weeks storage, show that the size of the Cu_2O became larger and their surfaces slightly roughened accompanied by small particles appeared (Fig. 7D). While there is no significant morphological changes for pTTh-Cu_2O (Fig. 7E), which partially confirms the photocorrosion could be effective restrained with the pTTh layer coating. Meanwhile, XRD analysis of Cu_2O and pTTh-Cu_2O photocathode after PEC tests and 2 weeks storage in Fig. 7F shows that dominate peaks were corresponding to Cu_2O, but no additional XRD peaks for CuO or metallic Cu can be found. Studies revealed that the morphology changes did not affect the crystal integrity of Cu_2O. These results verify that the as-prepared pTTh-Cu_2O photocathode exhibited a long-term stability and could be adopted as a suitable photocathode in PFC.

4. Conclusion

In summary, we have demonstrated an integrated power pack that can simultaneously realize solar and bioamss energy conversion through a quasi-solid-state PFC. The tandem PFC composed of an Au-TiO_2 NRAs photoanode and a pTTh-Cu_2O photocathode was adopted as energy harvesting unit for directly converting both chemical and solar energy into electricity. Thanks to the SPR effect, an excellent enhancement in the optical properties of the photoanode was obtained. The pTTh-Cu_2O photocathode by coating a pTTh film on the Cu_2O surface can greatly boost the photoresponse and resist photocorrosion. The assembled PFC enables the simultaneous utilization both solar energy and chemical energy, exhibiting a maximum power output density of 130 $\mu W{\cdot}cm^{-2}$ at + 0.6 V with a maximum open circuit potential of 0.78 V upon illumination. Such rational design of PFC system could also present a promising future for practical implementation in the field of organic wastes degradation and solar-driven water splitting.

Acknowledgements

This work was financial supported by the Major Program of Shandong Province Natural Science Foundation (ZR2017ZC0124), the program for Taishan Scholar of Shandong province (ts201712048), and

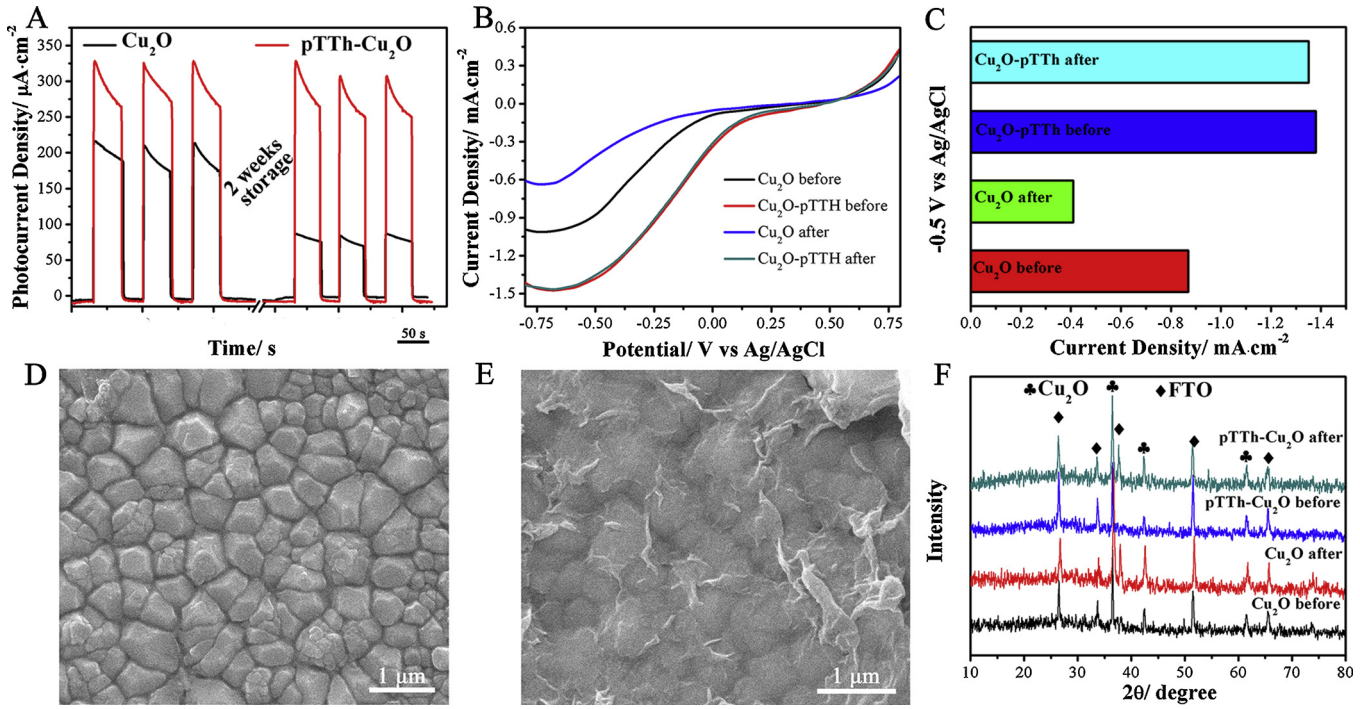

Fig. 7. (A) Cycle stability test on Cu_2O and pTTh-Cu_2O; LSV curves (B) and current histograms at fixed potentials (C) of different photocathodes before and after two weeks storage; SEM images of a Cu_2O film (D) and pTTh-Cu_2O (E) upon PEC measurement and two weeks sotrage; and (F) XRD patterns comparison of Cu_2O and pTTh-Cu_2O after PEC measurement and two weeks sotrage.

National Natural Science Foundation of China (21874055, 51632003). Supports from the 111 Project of International Corporation on Advanced Cement-based Materials (No. D17001) is greatly appreciated.

Appendix A. Supplementary data

Supplementary material related to this article can be found, in the online version, at doi:https://doi.org/10.1016/j.apcatb.2019.03.022.

References

[1] F. Qian, G. Wang, Y. Li, Solar-driven microbial photoelectrochemical cells with a nanowire photocathode, Nano Lett. 10 (2010) 4686–4691.
[2] Q. Wang, H. Chen, E. McFarland, L. Wang, Solar rechargeable batteries based on lead-organohalide electrolyte, Adv. Energy Mater. 5 (2015) 1501418.
[3] S.K. Kuk, R.K. Singh, D.H. Nam, R. Singh, J.K. Lee, C.B. Park, Photoelectrochemical reduction of carbon dioxide to methanol through a highly efficient enzyme cascade, Angew. Chem. Int. Ed. 56 (2017) 3827–3832.
[4] G.F. Brown, J. Wu, Third generation photovoltaics, Laser Photonics Rev. 3 (2009) 394–405.
[5] P. Lopez-Varo, L. Bertoluzzi, J. Bisquert, M. Alexe, M. Coll, J. Huang, J.A. Jimenez-Tejada, T. Kirchartz, R. Nechache, F. Rosei, Y. Yuan, Physical aspects of ferroelectric semiconductors for photovoltaic solar energy conversion, Phys. Rep. 653 (2016) 1–40.
[6] J. Li, X.Y. Feng, J.B. Fei, P. Cai, J.G. Huang, J.B. Li, Integrating photosystem II into a porous TiO_2 nanotube network toward highly efficient photobioelectrochemical cells, J. Mater. Chem. A 4 (2016) 12197–12204.
[7] Q. Zeng, J. Bai, J. Li, B.X. Zhou, Y.G. Sun, A low-cost photoelectrochemical tandem cell for highly-stable and efficient solar water splitting, Nano Energy 41 (2017) 225–232.
[8] Y. Yang, J. Gao, Z. Zhang, S. Xiao, H.H. Xie, Z.B. Sun, J.H. Wang, C.H. Zhou, Y.W. Wang, X.Y. Guo, P.K. Chu, X.F. Yu, Black phosphorus based photocathodes in wideband bifacial dye-sensitized solar cells, Adv. Mater. 28 (2016) 8937–8944.
[9] Z.Y. Zhou, Z.Y. Wu, Q. Xu, G. Zhao, A solar-charged photoelectrochemical wastewater fuel cell for efficient and sustainable hydrogen production, J. Mater. Chem. A 5 (2017) 25450–25459.
[10] W. Jian, X. Cheng, Y. Huang, Y. You, R. Zhou, T. Sun, J. Xu, Arrays of ZnO/MoS_2 nanocables and MoS_2 nanotubes with phase engineering for bifunctional photoelectrochemical and electrochemical water splitting, Chem. Eng. J. 328 (2017) 474–483.
[11] Y. Wang, J. Tang, Z. Peng, Y. Wang, D. Jia, B. Kong, A.A. Elzatahry, D. Zhao, G.F. Zheng, Fully solar-powered photoelectrochemical conversion for simultaneous energy storage and chemical sensing, Nano Lett. 14 (2014) 3668–3673.
[12] Z. Lan, J. Wu, S. Hao, J. Lin, M. Huang, Y. Huang, Template-free synthesis of closed-microporous hybrid and its application in quasi-solid-state dye-sensitized solar cells, Energy Environ. Sci. 2 (2009) 524–528.
[13] B.Q. Zhang, S.Y. Wang, W.J. Fan, W.G. Ma, Z.X. Liang, J.Y. Shi, S.J. Liao, C. Li, Photoassisted oxygen reduction reaction in H_2-O_2 fuel cells, Angew. Chem. Int. Ed. 55 (2016) 14748–14751.
[14] S. You, X. Gong, W. Wang, D. Qi, X. Wang, X. Chen, N. Ren, Enhanced cathodic oxygen reduction and power production of microbial fuel cell based on noble-metal-free electrocatalyst derived from metal-organic frameworks, Adv. Energy Mater. 6 (2016) 1501497.
[15] L. Zhang, L. Bai, M. Xu, L. Han, S.J. Dong, High performance ethanol/air biofuel cells with both the visible-light driven anode and cathode, Nano Energy 11 (2015) 48–55.
[16] B. Kolodziejczyk, O. Winther-Jensen, D.R. MacFarlane, B. Winther-Jensen, Conducting polymer alloys for photo-enhanced electro-catalytic oxygen reduction, J. Mater. Chem. 22 (2012) 10821–10826.
[17] B. Winther-Jensen, O. Winther-Jensen, M. Forsyth, D.R. Macfarlane, High rates of oxygen reduction over a vapor phase-polymerized PEDOT electrode, Science 321 (2008) 671–674.
[18] B. Zhang, W. Fan, T. Yao, S. Liao, A. Li, D. Li, M. Liu, J. Shi, S. Liao, C. Li, Design and fabrication of dual-photoelectrode fuel cell towards cost-effective electricity production from biomass derivatives, ChemSusChem 10 (2017) 99–105.
[19] W. Niu, T. Moehl, W. Cui, R. Wick-Joliat, L. Zhu, S.D. Tilley, Extended light harvesting with dual Cu_2O-based photocathodes for high efficiency water splitting, Adv. Energy Mater. 7 (2017) 1702323.
[20] C. Kim, K.M. Cho, A. Al-Saggaf, I. Gereige, H.T. Jung, Z-scheme photocatalytic CO_2 conversion on three-dimensional $BiVO_4$/carbon-coated Cu_2O nanowire arrays under visible light, ACS Catal. 8 (2018) 4170–4177.
[21] D. Liang, G. Han, Y. Zhang, S. Rao, S. Lu, H. Wang, Y. Xiang, Efficient H_2 production in a microbial photoelectrochemical cell with a composite Cu_2O/NiO_x photocathode under visible light, Appl. Energy 168 (2016) 544–549.
[22] C. Yang, P.D. Tran, P.P. Boix, P.S. Bassi, N. Yantara, L.H. Wong, J. Barber, Engineering a $Cu_2O/NiO/Cu_2MoS_4$ hybrid photocathode for H_2 generation in water, Nanoscale 6 (2014) 6506–6510.
[23] Y. Zhou, D. Shin, E. Ngaboyamahina, Q. Han, C.B. Parker, D.B. Mitzi, J.T. Glass, Efficient and stable Pt/TiO_2/CdS/$Cu_2BaSn(S,Se)_4$ photocathode for water electrolysis applications, ACS Energy Lett. 3 (2017) 177–183.
[24] J. Bai, Y.B. Li, R. Wang, K. Huang, Q.Y. Zeng, J.H. Li, B.X. Zhou, A novel 3D ZnO/Cu_2O nanowire photocathode material with highly efficient photoelectrocatalytic performance, J. Mater. Chem. A 3 (2015) 22996–23002.
[25] W.Z. Niu, L.P. Zhu, Y.C. Wang, Z.R. Lou, Z.Z. Ye, The interfacial study on the Cu_2O/Ga_2O_3/AZO/TiO_2 photocathode for water splitting fabricated by pulsed laser deposition, Catal. Sci. Technol. 7 (2017) 1602–1610.
[26] C.Y. Lin, Y.H. Lai, D. Mersch, E. Reisner, $Cu_2O|NiO_x$ nanocomposite as an inexpensive photocathode in photoelectrochemical water splitting, Chem. Sci. 3 (2012) 3482–3487.
[27] X.X. Chang, T. Wang, P. Zhang, Y.J. Wei, J.B. Zhao, J.L. Gong, Stable aqueous

photoelectrochemical CO_2 by a Cu_2O dark cathode with improved selectivity for carbonaceous products, Angew. Chem. Int. Ed. 55 (2016) 8840–8845.
[28] W. Fan, C. Chen, H. Bai, B. Luo, H. Shen, W. Shi, Photosensitive polymer and semiconductors bridged by Au plasmon for photoelectrochemical water splitting, Appl. Catal. B Environ. 195 (2016) 9–15.
[29] L. Zhang, Z. Xu, B. Lou, L. Han, X. Zhang, S.J. Dong, Visible-light-enhanced electrocatalysis and bioelectrocatalysis coupled in a miniature glucose/air biofuel cell, ChemSusChem 7 (2014) 2427–2431.
[30] Y. Yu, J.F. Zhai, Y. Xia, S.J. Dong, Single wearable sensing energy device based on photoelectric biofuel cells for simultaneous analysis of perspiration and illuminance, Nanoscale 9 (2017) 11846–11850.
[31] J. Gao, Y. Yang, Z. Zhang, J. Yan, Z. Lin, X. Guo, Bifacial quasi-solid-state dye-sensitized solar cells with poly(vinyl pyrrolidone)/polyaniline transparent counter electrode, Nano Energy 26 (2016) 123–130.
[32] P. Wang, S.M. Zakeeruddin, J.E. Moser, M.K. Nazeeruddin, T. Sekiguchi, M. Grätzel, A stable quasi-solid-state dye-sensitized solar cell with an amphiphilic ruthenium sensitizer and polymer gel electrolyte, Nat. Mater. 2 (2003) 402–407.
[33] J.H. Wu, Z. Lan, J.M. Lin, M.L. Huang, S.C. Hao, T. Sato, S. Yin, A novel thermosetting gel electrolyte for stable quasi-solid-state dye-sensitized solar cells, Adv. Mater. 19 (2007) 4006–4011.
[34] I.S. Cho, Z. Chen, A.J. Forman, D.R. Kim, P.M. Rao, T.F. Jaramillo, X. Zheng, Branched TiO_2 nanorods for photoelectrochemical hydrogen production, Nano Lett. 11 (2011) 4978–4984.
[35] H.X. Li, Z.D. Li, Y.H. Yu, Y.J. Ma, W.G. Yang, F. Wang, X. Yin, X.D. Wang, Surface-plasmon-resonance-enhanced photoelectrochemical water splitting from Au-nanoparticle-decorated 3D TiO_2 nanorod architectures, J. Phys. Chem. C 121 (2017) 12071–12079.
[36] J. Schneider, M. Matsuoka, M. Takeuchi, J.L. Zhang, Y. Horiuchi, M. Anpo, D.W. Bahnemann, Understanding TiO_2 photocatalysis: mechanisms and materials, Chem. Rev. 114 (2014) 9919–9986.
[37] M.M. Gao, L.L. Zhu, W.L. Ong, J. Wang, G.W. Ho, Structural design of TiO_2-based photocatalyst for H_2 production and degradation applications, Catal. Sci. Technol. 5 (2015) 4703–4726.
[38] J. Li, M.W.G. Hoffmann, H. Shen, C. Fabrega, J.D. Prades, T. Andreu, F. Hernandez-Ramirez, S. Mathur, Enhanced photoelectrochemical activity of an excitonic staircase in CdS@TiO_2 and CdS@anatase@rutile TiO_2 heterostructures, J. Mater. Chem. 22 (2012) 20472–20476.
[39] J. Li, S.K. Cushing, P. Zheng, T. Senty, F. Meng, A.D. Bristow, A. Manivannan, N. Wu, Solar hydrogen generation by a CdS-Au-TiO_2 sandwich nanorod array enhanced with Au nanoparticle as electron relay and plasmonic photosensitizer, J. Am. Chem. Soc. 136 (2014) 8438–8449.
[40] S.W. Lee, Y.S. Lee, J. Heo, S.C. Siah, D. Chua, R.E. Brandt, S.B. Kim, J.P. Mailoa, T. Buonassisi, R.G. Gordon, Improved Cu_2O-based solar cells using atomic layer deposition to control the Cu oxidation state at the p-n junction, Adv. Energy Mater. 4 (2014) 1301916.
[41] Z. Bai, Y. Zhang, A Cu_2O/Cu_2S-ZnO/CdS tandem photoelectrochemical cell for self-driven solar water splitting, J. Alloys Compd. 698 (2017) 133–140.
[42] S. Shyamal, P. Hajra, H. Mandal, J.K. Singh, A.K. Satpati, S. Pande, C. Bhattacharya, Effect of substrates on the photoelectrochemical reduction of water over cathodically electrodeposited p-type Cu_2O thin films, ACS Appl. Mater. Interfaces 7 (2015) 18344–18352.
[43] P. Zhong, X.H. Ma, X.P. Chen, R. Zhong, X.H. Liu, D.J. Ma, M.L. Zhang, Z.M. Li, Morphology-controllable polycrystalline TiO_2 nanorod arrays for efficient charge collection in dye-sensitized solar cells, Nano Energy 16 (2015) 99–111.
[44] H. Li, Z. Su, S. Hu, Y. Yan, Free-standing and flexible Cu/Cu_2O/CuO heterojunction net: a novel material as cost-effective and easily recycled visible-light photocatalyst, Appl. Catal. B Environ. 207 (2017) 134–142.
[45] H. Chen, M. Zhou, T. Wang, F. Li, Y.X. Zhang, Construction of unique cupric oxide-manganese dioxide core-shell arrays on a copper grid for high performance supercapacitors, J. Mater. Chem. A 4 (2016) 10786–10793.
[46] H.M. Shi, S. Zhang, X.P. Zhu, Y. Liu, T. Wang, T. Jiang, G. Zhang, H.G. Duan, Uniform gold-nanoparticle-decorated {001}-faceted anatase TiO_2 nanosheets for enhanced solar-light photocatalytic reactions, ACS Appl. Mater. Interfaces 9 (2017) 36907–36916.
[47] L. Wang, H. Hu, N.T. Nguyen, Y. Zhang, P. Schmuki, Y. Bi, Plasmon-induced hole-depletion layer on hematite nanoflake photoanodes for highly efficient solar water splitting, Nano Energy 35 (2017) 171–178.
[48] Z. Zhang, L. Zhang, M.N. Hedhili, H. Zhang, P. Wang, Plasmonic gold nanocrystals coupled with photonic crystal seamlessly on TiO_2 nanotube photoelectrodes for efficient visible light photoelectrochemical water splitting, Nano Lett. 13 (2013) 14–20.
[49] Z. Zhang, P. Wang, Highly stable copper oxide composite as an effective photocathode for water splitting via a facile electrochemical synthesis strategy, J. Mater. Chem. 22 (2012) 2456–2464.
[50] J.S. DuChene, B.P. Williams, A.C. Johnston-Peck, J. Qiu, M. Gomes, M. Amilhau, D. Bejleri, J. Weng, D. Su, F. Huo, E.A. Stach, W.D. Wei, Elucidating the sole contribution from electromagnetic near-fields in plasmon-enhanced Cu_2O photocathodes, Adv. Energy Mater. 6 (2016) 1501250.
[51] Z.H. Zhang, R. Dua, L.B. Zhang, H.B. Zhu, H.N. Zhang, P. Wang, Carbon-layer-protected cuprous oxide nanowire arrays for efficient water reduction, ACS Nano 7 (2013) 1709–1717.
[52] L. Zheng, S. Han, H. Liu, P. Yu, X. Fang, Hierarchical MoS_2 nanosheet@TiO_2 nanotube array composites with enhanced photocatalytic and photocurrent performances, Small 12 (2016) 1527–1536.
[53] L. Pan, J.H. Kim, M.T. Mayer, M.K. Son, A. Ummadisingu, J.S. Lee, A. Hagfeldt, J. Luo, M. Grätzel, Boosting the performance of Cu_2O photocathodes for unassisted solar water splitting devices, Nat. Catal. 1 (2018) 412–420.
[54] Q. Zeng, J. Bai, J. Li, Y. Li, X. Li, B. Zhou, Combined nanostructured Bi_2S_3/TNA photoanode and Pt/SiPVC photocathode for efficient self-biasing photoelectrochemical hydrogen and electricity generation, Nano Energy 9 (2014) 152–160.
[55] Y.C. Pu, G. Wang, K.D. Chang, Y. Ling, Y.K. Lin, B.C. Fitzmorris, C.M. Liu, X. Lu, Y. Tong, J.Z. Zhang, Y.J. Hsu, Y. Li, Au nanostructure-decorated TiO_2 nanowires exhibiting photoactivity across entire UV-visible region for photoelectrochemical water splitting, Nano Lett. 13 (2013) 3817–3823.
[56] S. Shyamal, P. Hajra, H. Mandal, A. Bera, D. Sariket, A.K. Satpati, M.V. Malashchonak, A.V. Mazanik, O.V. Korolik, A.I. Kulak, E.V. Skorb, A. Maity, E.A. Streltsov, C. Bhattacharya, Eu modified Cu_2O thin films: Significant enhancement in efficiency of photoelectrochemical processes through suppression of charge carrier recombination, Chem. Eng. J. 335 (2018) 676–684.
[57] Y. Chen, L. Wang, W. Wang, M. Cao, Enhanced photoelectrochemical properties of ZnO/ZnSe/CdSe/Cu_{2-x}Se core-shell nanowire arrays fabricated by ion-replacement method, Appl. Catal. B Environ. 209 (2017) 110–117.
[58] Y. Hu, X. Yan, Y. Gu, X. Chen, Z. Bai, Z. Kang, F. Long, Y. Zhang, Large-scale patterned ZnO nanorod arrays for efficient photoelectrochemical water splitting, Appl. Surf. Sci. 339 (2015) 122–127.
[59] Y. Dai, Y. Sun, J. Yao, D. Ling, Y. Wang, H. Long, X. Wang, B. Lin, T.H. Zeng, Y. Sun, Graphene-wrapped TiO2 nanofibers with effective interfacial coupling as ultrafast electron transfer bridges in novel photoanodes, J. Mater. Chem. A 2 (2014) 1060–1067.
[60] S.J. Hong, S. Lee, J.S. Jang, J.S. Lee, Heterojunction BiVO4/WO_3 electrodes for enhanced photoactivity of water oxidation, Energy Environ. Sci. 4 (2011) 1781–1787.
[61] R. Tang, S. Zhou, Z. Yuan, L. Yin, Metal-organic framework derived Co_3O_4/TiO_2/Si heterostructured nanorod array photoanodes for efficient photoelectrochemical water oxidation, Adv. Funct. Mater. 27 (2017) 1701102.
[62] S.J.A. Moniz, J. Zhu, J. Tang, 1D Co-Pi modified BiVO4/ZnO junction cascade for efficient photoelectrochemical water cleavage, Adv. Energy Mater. 4 (2014) 1301590.
[63] P.P. Jha, P. Guyot-Sionnest, Photoluminescence switching of charged quantum dot films, J. Phys. Chem. C 111 (2007) 15440–15445.
[64] Y.F. Zhu, D.H. Fan, W.Z. Shen, Chemical conversion synthesis and optical properties of metal sulfide hollow microspheres, Langmuir 24 (2008) 11131–11136.
[65] R. Tang, S. Zhou, L. Zhang, L.W. Yin, Metal-organic framework derived narrow bandgap cobalt carbide sensitized titanium dioxide nanocage for superior photoelectrochemical water oxidation performance, Adv. Funct. Mater. 28 (2018) 1706154.
[66] Y. Zheng, Z. Yu, H. Ou, A.M. Asiri, Y. Chen, X. Wang, Black phosphorus and polymeric carbon nitride heterostructure for photoinduced molecular oxygen activation, Adv. Funct. Mater. 28 (2018) 1705407.
[67] L. Xia, J. Bai, J. Li, Q. Zeng, X. Li, B. Zhou, A highly efficient $BiVO_4/WO_3$/W heterojunction photoanode for visible-light responsive dual photoelectrode photocatalytic fuel cell, Appl. Catal. B Environ. 183 (2016) 224–230.
[68] Q. Chen, J. Li, X. Li, K. Huang, B. Zhou, W. Cai, W. Shangguan, Visible-light responsive photocatalytic fuel cell based on WO_3/W photoanode and Cu_2O/Cu photocathode for simultaneous wastewater treatment and electricity generation, Environ. Sci. Technol. 46 (2012) 11451–11458.
[69] R.O. Takakura, T. Ueno, K. Shi, X. Kondo, T. Masuda, H. Misawa, Water splitting using a three-dimensional plasmonic photoanode with titanium dioxide nano-tunnels, Green Chem. 19 (2017) 2398–2405.
[70] Y. Liu, F. Ren, S. Shen, Y. Fu, C. Chen, C. Liu, Z. Xing, D. Liu, X. Xiao, W. Wu, X. Zheng, Y. Liu, C. Jiang, Efficient enhancement of hydrogen production by Ag/Cu_2O/ZnO tandem triple-junction photoelectrochemical cell, Appl. Phys. Lett. 106 (2015) 123901.
[71] X. Chen, H. Sun, Z. Yang, G. Guan, Z. Zhang, L. Qiu, H. Peng, A novel “energy fiber” by coaxially integrating dyesensitized solar cell and electrochemical capacitor, J. Mater. Chem. A 2 (2014) 1897–1902.
[72] X.H. Xia, Z.L. Ku, D. Zhou, Y. Zhong, Y.Q. Zhang, Y.D. Wang, M.J. Huang, J.P. Tu, H.J. Fan, Perovskite solar cell powered electrochromic batteries for smart windows, Mater. Horiz. 3 (2016) 588–595.
[73] T. Wang, Y. Wei, X. Chang, C. Li, A. Li, S. Liu, J. Zhang, J. Gong, Homogeneous Cu_2O p-n junction photocathodes for solar water splitting, Appl. Catal. B-Environ. 226 (2018) 31–37.